 Cytometry 35:203–213 (1999)

Quantitative Analysis of Cytokeratin Network Topology in the MCF7 Cell Line

Stéphanie Portet,[1]* Jany Vassy,[1] Michael Beil,[2] Guy Millot,[3] Abdelhamid Hebbache,[1] Jean Paul Rigaut,[1] and Damien Schoëvaërt[1]

[1]Laboratoire d'Analyse d'Images en Pathologie Cellulaire, Institut Universitaire d'Hématologie, Hôpital Saint Louis, Paris, France
[2]Department of Internal Medicine I, University of Ulm, Ulm, Germany
[3]Laboratoire de Pharmacologie, Institut Universitaire d'Hématologie, Hôpital Saint Louis, Paris, France

Received 23 April 1998; Revision Received 17 August 1998; Accepted 14 October 1998

Background: In the MCF7 human breast cancer cell line, several patterns of cytokeratin networks are observed, depending on the intracellular localization. Our hypothesis is that architectural variations of cytokeratin networks depend on local tensions or forces appearing spontaneously in the cytoplasm. The aim of this work was to discriminate between the different patterns and to quantitate these variations.

Materials and Methods: Image analysis procedures were developed to extract cytokeratin filament networks visualized by immunofluorescence and confocal microscopy. Two methods were used to segment sets of curvilinear objects. The first, the ''mesh-approach,'' based on classical methods of mathematical morphology, takes into account global network topology. The second, the ''filament-approach'' (novel), is meant to account for individual element morphology. These methods and their combination allow the computation of several features at two levels of geometry: global (network topology) and local (filament morphology).

Results: Variations in cytokeratin networks are characterized by their connectivity, density, mesh structure, and filament shape. The connectivity and the density of a network describe its location in a local ''stress-force'' zone or in a ''relaxed'' zone. The mesh structure characterizes the intracellular localization of the network. Moreover, the filament shape reflects the intracellular localization and the occurrence of a ''stress-force'' zone.

Conclusions: These features permitted the quantitation of differences within the network patterns and within the specific filament shapes according to the intracellular localization. Further experiments on cells submitted to external forces will test the hypothesis that the architectural variations of intermediate filaments reflect intracytoplasmic tensions. Cytometry 35:203–213, 1999. © 1999 Wiley-Liss, Inc.

Key terms: cytoskeleton; cytokeratin; tensegrity; confocal microscopy; image analysis; curvilinear structures; network topology; filament morphology

Recent reports assume that not only chemical but also mechanical influences from the cellular environment could have profound effects on gene activity and act on cell differentiation and proliferation (1–4). Both physical and biochemical signal transductions have been used to explain the mechanical influences of the extracellular matrix (5). Structural transductions involve an ''extended tissue matrix'' which includes extracellular matrix, nuclear matrix, and cytoskeleton (6–9). Cytoplasmic cytoskeleton would be an intermediate between extracellular and nuclear matrix, and alterations of the nuclear matrix influence finally the transcriptional activity of specific genes (10,11). Physicochemical properties, coiled-coil structure (reviewed by Stewart (12)), and viscoelastic properties (13) of intermediate filaments suggest that they may play a role in determining the stiffness of epithelial cells (14,15). They may therefore be the best candidates, among other components of the cytoskeleton, for a possible structural and mechanical transduction of signals from the environment (16). Assuming that mechanotransduction is mediated by the cytoskeleton, physical changes in the cellular environment would be reflected by structural variations of cytoskeleton architecture and, more specifically, of intermediate filaments.

The MCF7 human breast cancer cell line was widely investigated, especially for studying growth regulation. These cells maintained estrogen receptors and expressed cytokeratin but not vimentin as intermediate filaments (17,18). In MCF7, local intracytoplasmic variations in cytokeratin networks are observed (19), and different network patterns appear in specific intracytoplasmic loca-

Grant sponsor: Ligue Nationale contre le Cancer; Grant sponsor: Centre National d'Etudes Spatiales.

*Correspondence to: Stéphanie Portet, Laboratoire AIPC, UP7, Institut d'Hématologie, Hôpital Saint Louis, 1 Avenue Claude Vellefaux, 75475 Paris Cedex 10, France.
E-mail: portet@chu-stlouis.fr

tions. Our hypothesis is that these architectural changes (network connectivity, density and mesh structure, and filament shape) probably depend on local cytoplasmic tensions or forces. In a further step, we will investigate variations induced experimentally by physical changes of the cellular environment (work in progress).

In previous work (20–22), image analysis procedures were defined in order to describe variations of cytokeratin networks in rat hepatocytes during fetal development. These approaches were not designed to discriminate between different patterns inside individual cells. In the present work, we developed image analysis procedures allowing the detection of subtle local variations in cytokeratin networks of MCF7, depending on the intracellular localization. High-resolution confocal microscopy of immunofluorescent visualization of cytokeratins and computerized image analysis offer the opportunity of such a study.

The cytokeratin network can be regarded at two levels, global (network topology: properties of the set of elements) and local (filament morphology: properties of the elements). We developed two methods of segmentation taking into account these two levels, respectively: 1) the ''mesh-approach,'' based on mathematical morphology, relying on the cytoskeletal network viewed as a connected graph; and 2) the novel ''filament approach,'' relying on the individual elements of the network. A combination of the two methods provides a powerful tool for analyzing cytokeratin networks. Variations in cytokeratin networks can be characterized by 1) the degree of connectivity, 2) the density of the network, 3) the mesh structure, and 4) the filament shape. The aim of the present work was to quantitate the local variations of cytokeratin architectures and to discriminate between the different patterns observed: three patterns, corresponding to three specific intracytoplasmic localizations, were selected and compared by means of a nonparametric Mann-Whitney test with respect to topological and morphological features.

MATERIALS AND METHODS

Cell Cultures

The MCF7 cell line, derived from a human breast carcinoma (23), was grown for 24 h at 37°C in a 5% CO_2 atmosphere, in Dulbecco's modified Eagle's medium (DMEM, Gibco), supplemented with 10% fetal calf serum (Boeringer, Mannheim, Germany), containing 2 mM glutamine (Gibco), 50 U/ml penicillin, and 50 µg/ml streptomycin (Gibco).

Immunofluorescence Staining

Cell cultures were fixed for 10 min at 20°C in 4% paraformaldehyde diluted in 0.1 M phosphate buffer.

The indirect immunolocalization procedure was used. After 15 min washing in phosphate-buffered saline (PBS), a 30-min preincubation was carried out with 60 mg/ml bovine serum albumin (Sigma, France) and 0.1% saponin (Sigma) to avoid nonspecific labeling. Cells were incubated overnight at 4°C in a mouse monoclonal antibody anti-C8 (C-5301, Sigma) diluted at 1/50 in PBS containing 0.1% saponin. After washing for 3 × 10 min in PBS, mouse IgG were visualized by a 2-h incubation at 20°C in 1/50 lissamine rhodamine (LRSC) and conjugated donkey anti-mouse IgG (715–085150, Jackson Laboratories).

After washing, cell cultures were mounted in Mowiol (Calbiochem, France).

Confocal Microscopy and Image Acquisition

Fluorescent cytokeratin filaments were visualized by an MRC-600 (BioRad, UK) confocal scanning laser system, mounted on a Nikon microscope equipped with a Plan Apochromat immersion objective (×60) with a high numerical aperture (1.4).

The 514-nm wavelength of the multiple-line argon ion laser beam (25 mW) was used for LRSC excitation. Red fluorescence was detected using a long-pass filter (OG 550).

Image acquisitions were carried out using discrete photon counting (24) by the Comos software package (BioRad), with a scan speed of 1 frame/s (768 × 512 pixels). Fast photon counting allows a sharp visualization of weak labels even with the highest (x , y) sampling density (11 pixels/µm). Each confocal image of 768 × 512 pixels and 256 gray levels was obtained by averaging 20 frames.

Fifty images (768 × 512 pixels) were collected where several architectural patterns of cytokeratin network appeared (Fig. 1b). From these, smaller images (100 × 100 pixels) were selected according to intracytoplasmic localization: 1) in hemidesmosome (extracellular matrix-cell contact) or desmosome (cell-cell contact) zones (Fig. 1b,c), 2) in leading margin zones of spreading cell, without intercellular contact (Fig. 1a,d), and 3) in zones around the nucleus (Fig. 1b, e).

Twenty images (100 × 100 pixels, 83 μm^2), for each location observed, were studied (Fig. 1c–e).

Image Analysis

In this preliminary work, with culture cells flattened and the zones under investigation located in a specific plane (near the nuclear envelope or areas of substratum-cell contacts, Fig. 1a), image analysis procedures were carried out on two-dimensional (2D) images. A new method for extracting filament structures was developed. This method is based on two geometry levels, the mesh level (network topology: properties of the set of elements) and the filament level (filament morphology: properties of the elements). The mesh level represents a global approach (''mesh-approach''), while the filament level deals with features of mesh elements (''filament-approach'').

All programs were developed using the software package AMBA (IBSB, Berlin, Germany), running on a 300-Mhz Pentium II.

The ''Mesh-Approach''

The gray scale image I is considered as a topographic surface, where the altitude of a pixel is given by its gray value (25). The filament network is represented as the network of crest lines. Supposing that the network is a

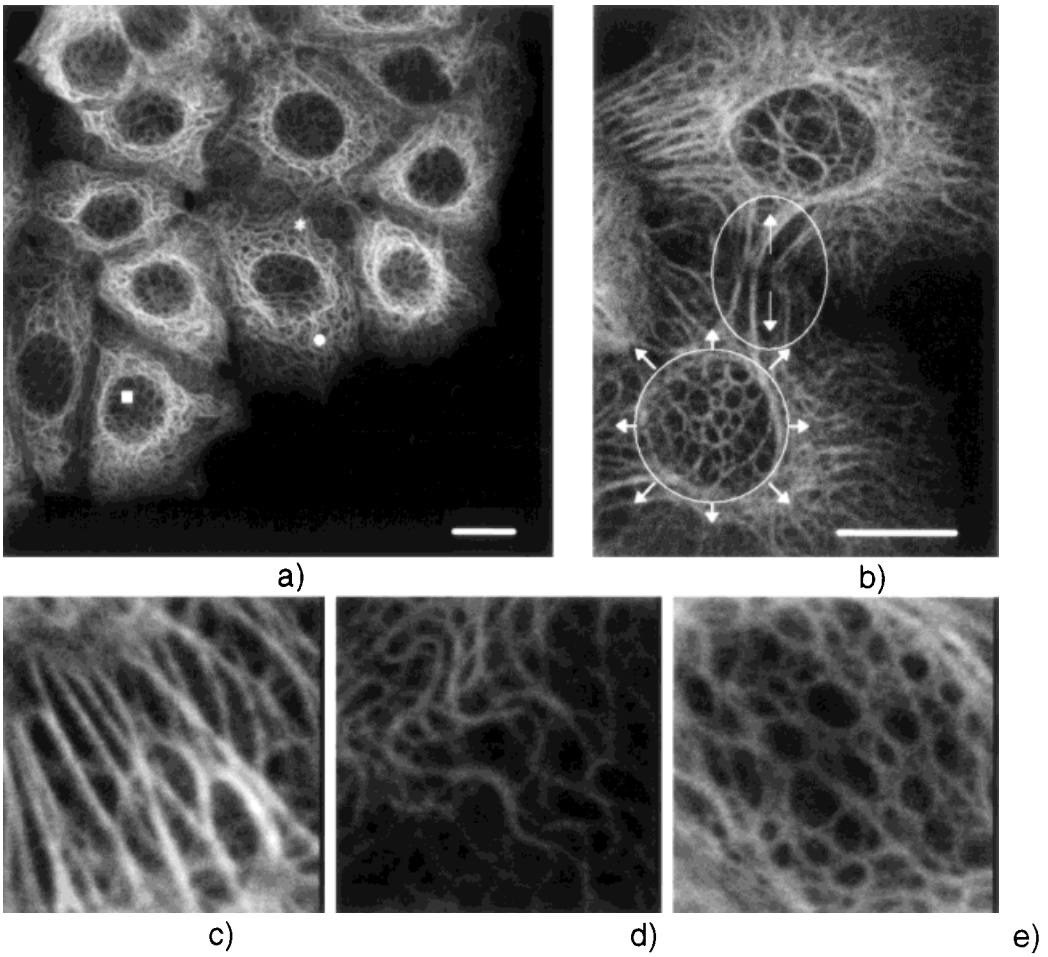

FIG. 1. **a:** The cytokeratin (C_8) network in MCF7 is formed by cross-linked filaments. ● marks the leading margin zones of spreading cell, without contact. ■ labels the zones around the nucleus. * spots the hemidesmosome (extracellular matrix-cell contact) or desmosome (cell-cell contact) zones. Low magnification (4 pixels/μm), scale bar is 10 μm. **b:** Two cells connect to each other in desmosome zones (inside the ellipse). The confocal section is achieved in a plane located under the nucleus (inside the circle) and, therefore, the C_8 network is observed. Arrows indicate the direction of the supposed local intracytoplasmic stress-forces in a selected area. High magnification (11 pixels/μm), scale bar is 10 μm. c–e: Focusing on the three patterns of cytokeratin observed in MCF7. **c:** Cytokeratin filaments in desmosome zone: ''rectilinear'' pattern. **d:** Cytokeratin filaments in a spreading zone of cytoplasm: ''wave-like'' pattern. **e:** Cytokeratin filaments around the nucleus: ''alveolar'' pattern. Resolution is 11 pixels/μm; each image represents an area of 83μm^2.

connected graph, the aim of this approach is to extract its topological features. The watershed method seems to be appropriate, because it results in a pixel-width line preserving the summits of images (26). The watershed segmentation is prone to oversegmentation due to noise effects. Thus, we performed a preprocessing step. It consists of a closing (27,28) with a structuring element whose size depends on the object width (Fig. 2a–c).

Following preprocessing, the watershed method for gray scale images is applied, using an iterative homotopic thinning operation until idempotence (29). This thinning lowers the gray scale of pixels belonging to the side of crests, but does not affect gray values of summits and valleys. Finally, a gray scale image with the crest lines (water partings) surrounding homogeneous regions (watersheds) is obtained (Fig. 2d–f).

Despite the preprocessing, the result is still oversegmented. Therefore, a region-merging algorithm has been developed and applied in addition (see Appendix 1).

The result of the ''mesh-approach'' is a unit-width mainly connected line (Fig. 2g–i).

Region-merging algorithm. The region-merging algorithm compares two neighboring regions and unifies them by erasing water partings. The gray scale altitudes of two adjacent regions A1 and A2 are compared. If the altitude difference A1–A2 is lower than a threshold R, A1 and A2 are compared with the mean altitude AL along the crest line separating them. If min(AL–A1 , AL–A2) is lower than a threshold M, the crest line section is erased. The sensitivity of the algorithm depends on the parameters R and M defined by the user (see Appendix 1).

The ''Filament-Approach''

In order to preserve the morphology of filaments, we designed a novel two-step method, the ''filament-approach.'' The gray scale image is first filtered using a nonlinear filter Ψ (see Appendix 2), which was designed

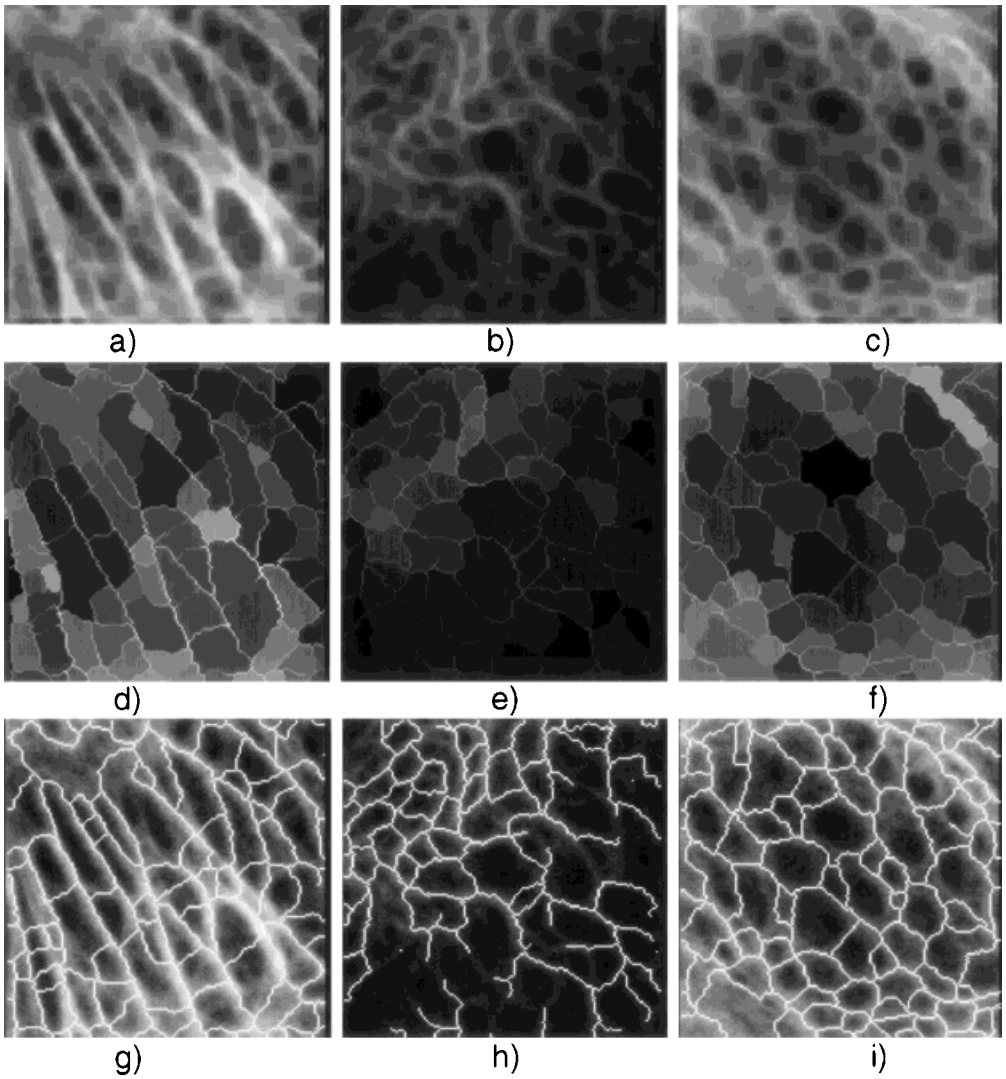

FIG. 2. Steps of the ''mesh-approach'' for the three patterns. **a,d,g:** ''rectilinear'' pattern. **b,e,h:** ''wave-like'' pattern. **c,f,i:** ''alveolar'' pattern. a–c: Gray level morphological closing with a structuring element of size 5×5, since the filaments within the gray scale images have a mean width of 7 pixels (Fig. 1c–e). d–f: Results of watershed method for gray scale images: gray scale images with the crest lines (water parting) surrounding homogeneous regions (watersheds). g–i: Results of ''mesh-approach'' after the region-merging algorithm step.

to detect local maxima thicker than one pixel. In the second step, the line elements (curvilinear elements) are reconstructed in a dynamic thresholding procedure combined with mathematical morphology operations (see Appendix 3). The results of the ''filament-approach'' are represented in Figure 3d–f.

Nonlinear filter of the "filament-approach." A simple thresholding is first used to suppress background noise. The filter Ψ is composed of two steps, a selection step and a decision step (see Appendix 2). The selection step processes the gray values to characterize the topology within a neighborhood. The pixels are assigned to either line pixels or background pixels in the decision step. The final image, obtained by application of Ψ, is a gray scale image of the crest lines neighborhood (Fig. 3a–c).

Reconstruction of the curvilinear elements (filaments). The last step of the ''filament-approach'' consists of a dynamic thresholding combined with mathematical morphology transformations. This procedure contains a variable decision domain, i.e., the decision rules depend on the gray values. With this method, the lower the threshold value, the smaller the decision domain, i.e.. the darkest pixels are unfavored. The pixels selected according to the criterion ϕ are marked for further processing (see Appendix 3). A circular dilation step allows the restoration of connectivity without favoring a specific direction (30). To obtain a network of digital lines, the last step is an anchored skeletonization (20).

Combination of Methods

Since both methods preserve complementary network properties (topology of network for the ''mesh-approach'' and morphology of individual element for the ''filament-

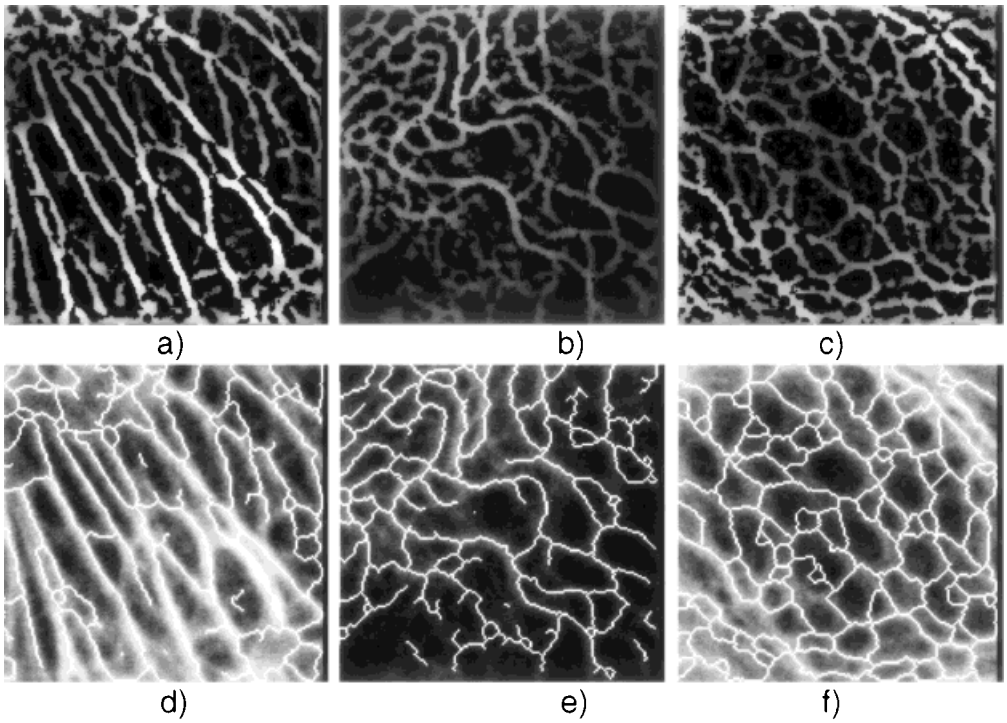

FIG. 3. Steps of ''filament-approach'' for the three patterns. **a, d:** ''rectilinear'' pattern. **b, e:** ''wave-like'' pattern. **c, f:** ''alveolar'' pattern. a–c: Results of the nonlinear filter of the ''filament-approach.'' d–f: Results of ''filament-approach'' after the reconstruction of the curvilinear elements.

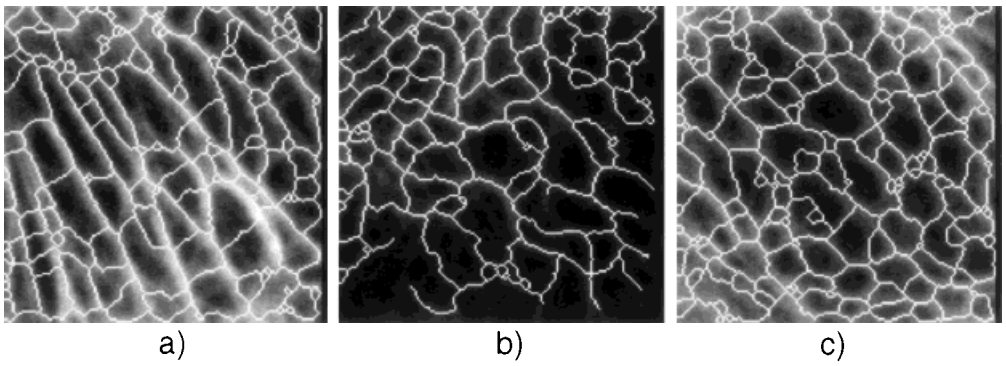

FIG. 4. Results of the combination of methods for the three patterns. **a:** ''rectilinear'' pattern. **b:** ''wave-like'' pattern. **c:** ''alveolar'' pattern. The combination of methods preserves both network topology and individual filament morphology.

approach''), the two methods were combined in order to take advantage of the two properties.

Due to the difference in the segmentation process, a simple union of the two images does not provide unit-width lines. Therefore, the image resulting from an overlay has to be further processed to obtain digital lines. This is performed by a dilation followed by a binary skeletonization (28):

$$S_c = (((S_m \cup S_f) \oplus B)OL),$$

where S_m is a ''mesh-approach'' segmented image, S_f is a ''filament-approach'' segmented image, B is a structuring element, and L is a Golay alphabet structuring element (30). The result S_c of the combination is shown in Figure 4a–c.

Feature Extraction

The following features are defined to describe the topology and morphology of the network:

number of connection points	N_{cp}
total length of detected filaments	L_f
number of regions surrounded by detected filaments	N_r
areas of regions surrounded by detected filaments	A_r
curvature	C

In order to obtain standard values for the feature curvature (C), we interactively selected filaments which were characteristic for the various patterns. From each ''filament-approach'' segmented image, we extracted a filament of characteristic shape. The extraction was obtained by an interactive program. First, the starting point of the filament was chosen. The program carried out the tracking of the filament from the starting point to the first branching point. From each branching point met, the user must decide which branch to follow.

From these extracted filaments, the curvature distributions for the three specific shapes were obtained. The computation of the curvature was achieved with the classical geometrical method of construction of the osculating circle (31). The curvature sign depends on the location of the osculating circle relative to the curve.

In addition to the primary features, we computed the following features: connecting index (I_c), mean length of filaments enclosing a region (L_r), and mean elongation factor (E_f) (30).

$$I_c = \frac{L_f}{N_{cp}},$$

$$L_r = 2 \times \frac{L_f}{N_r},$$

$$E_f = \frac{d\ \max}{d\ \min},$$

d max and *d* min are the Feret diameters in two directions (30).

The seven features (N_{cp}, I_c, L_f, N_r, A_r, L_r, and E_f) were determined from the combination of methods. On the other hand, the computation of the curvature (C) was determined from the ''filament-approach'' results.

Statistical Analysis

With the aim of discriminating between two patterns depending on the topological and morphological features, we chose to use the Mann-Whitney test because this test allows the test of equality of location of two feature samples (32). The test of equality of location of two feature samples is obtained by showing that one of two random variables, representing the feature of a given pattern, is stochastically larger than the other, representing the feature of another pattern (33): a random variable A is said to be stochastically larger than a random variable B if $\forall z$ $P(B \leq z) \leq P(A \leq z)$. In others words, the realizations of the random variable are larger than the realizations of the random variable B in probability.

The level of significance for each comparison was 0.05.

The statistical analysis was performed using the Stat2005 software package (Unilog, Grenoble, France).

RESULTS

Architectural Changes of Cytokeratin Networks

Figure 1a represents a global view of the cytokeratin (C_8) network in MCF7 cells: * spots the hemidesmosome (extracellular matrix-cell contact) or desmosome (cell-cell contact) zones, ■ labels the zones around the nucleus, and ● marks the leading margin zones of spreading cell, without contact. In Figure 1b, two cells connect to each other in desmosome zones (inside the ellipse). At a higher magnification (Fig. 1c–e), local architectural changes correspond to at least three patterns of networks: ''rectilinear,'' ''wave-like,'' and ''alveolar'' patterns. The ''rectilinear'' pattern appears in desmosome zones and is composed of unidirectionally-oriented objects, like straight lines (anisotropic pattern) (Fig. 1c). It could be related to tension created when adjacent cells connect to each other (Fig. 1a*, Fig. 1b inside the ellipse: arrows indicate the direction of supposed forces). A ''wave-like'' pattern appears in isolated cells and is formed by cross-linked objects comparable to curvilinear structures (Fig. 1d). It seems to be present in ''relaxed'' zones of cytoplasm, when cells are isolated and hemidesmosomes are probably not yet established (Fig. 1a ●). The ''alveolar'' pattern forms a basket-like network around the nucleus and is composed of adjacent-linked closed curves (isotropic pattern) (Fig. 1e). The ''alveolar'' pattern seems to maintain nucleus position and probably to protect it from compression (Fig. 1a ■, Fig. 1b inside the circle).

Network Extraction

The segmented images of cytokeratin represent networks of interconnected curvilinear or linear structures. The three segmentation methods provide a skeleton, i.e., a pixel-width line representing the network (Figs. 2g–i, 3d–f, 4a–c).

The cytokeratin networks have two levels of organization: 1) the higher level, corresponding to the network topology (the ''mesh-approach'' correctly models the topology); and 2) the lower level, corresponding to the morphology of the individual filaments. The ''filament-approach'' allows an efficient modeling of the individual filaments. A characteristic shape filament can be extracted from each pattern. It resembles a straight line in the ''rectilinear'' pattern (Fig. 1c), a curve in the ''wave-like'' pattern (Fig. 1d), and a circle in the ''alveolar'' pattern (Fig. 1e).

Feature Analysis

The results of statistical analysis are summarized in Table 1.

Topological Features

Both the number of connection points (N_{cp}) and the connecting index (I_c) characterize the connectivity of a network. The total length of detected filaments (L_f) and the number of regions surrounded by detected filaments (N_r) describe the network density. The mesh structure is represented by three features: areas of regions surrounded by detected filaments (A_r), mean length of filaments enclosing a region (L_r), and mean elongation factor (E_f).

Table 1
*Number of Connection Points (N_{cp}), Connecting Index (I_c), Total Length of Detected Filament (L_f), Number of Regions (N_r), Areas of Regions (A_r), Mean Length of Filaments Enclosing a Region (L_r), and Mean Elongation Factor (E_f) in the Combination of Methods Depending on the Three Patterns**

	(R) Rectilinear pattern (n = 20) (Mean ± SD)	(W) Wave-like pattern (n = 20) (Mean ± SD)	(A) Alveolar pattern (n = 20) (Mean ± SD)	Mann-Whitney test *P* (significant test if $P < .05$)		
(N_{cp})	99.9 ± 37.4	74.1 ± 19.2	111.9 ± 20.7	(R-W)	.026	S
				(R-A)	.35	NS
				(W-A)	<.0001	S
(I_c)	10.5 ± 3.3	12.5 ± 1.9	10.1 ± 1.3	(R-W)	.014	S
				(R-A)	.507	NS
				(W-A)	.00015	S
(L_f)	1,027.1 ± 235.4	895.7 ± 134.7	1,110.2 ± 87.2	(R-W)	.025	S
				(R-A)	.33	NS
				(W-A)	<.0001	S
(N_r)	25.6 ± 7.7	21.5 ± 6.7	30.7 ± 3.6	(R-W)	.076	NS
				(R-A)	.053	NS
				(W-A)	<.0001	S
(A_r)	310.3 ± 467.9	392.4 ± 503.1	254.7 ± 154.5	(R-W)	.0005	S
				(R-A)	.24	NS
				(W-A)	.006	S
(L_r)	41.5 ± 5.9	44.5 ± 10.9	36.5 ± 4.2	(R-W)	.685	NS
				(R-A)	.0028	S
				(W-A)	.0026	S
(E_f)	1.6 ± 0.8	1.5 ± 0.9	1.55 ± 1.1	(R-W)	.333	NS
				(R-A)	.0009	S
				(W-A)	.038	S
(C)	−0.0001 ± 0.02	−0.002 ± 0.04	0.06 ± 0.03	(R-W)	.0076	S
				(R-A)	<.0001	S
				(W-A)	<.0001	S

*Curvature (C) in the ''filament-approach'' depends on the three patterns. S, significant test; NS, non-significant test.

Network Connectivity

Number of connection points (N_{cp}). When combining the two methods, the Mann-Whitney test showed that both ''rectilinear'' and ''alveolar'' pattern distributions were stochastically larger (see Statistical Analysis) than the ''wave-like'' pattern distribution (Table 1). On the other hand, no significant difference was found between ''alveolar'' and ''rectilinear'' patterns.

The ''wave-like'' pattern seems to be less connected than the other patterns. The connectivity of the ''alveolar'' pattern is not unlike that of the ''rectilinear'' pattern.

Connecting index (I_c). The connecting index is computed by using the combination of the two methods. The larger the connecting index, the looser the connections of the network (Table 1). The ''wave-like'' pattern distribution is stochastically larger than both the ''rectilinear'' and ''alveolar'' pattern distributions: in the ''wave-like'' pattern, the network is less connected. The connecting index behaves in the same way in the ''alveolar'' and ''rectilinear'' patterns.

The two features of the network connectivity behave in the same way. Both patterns (''rectilinear'' and ''alveolar'') apparently display the same behavior. ''Wave-like'' patterns are less connected than the two others.

Network Density

Total length of detected filaments (L_f). The total length of detected filaments (Table 1) shows significant differences between the ''rectilinear'' and the ''wave-like'' patterns, and between the ''alveolar'' and the ''wave-like'' patterns. The ''rectilinear'' and ''alveolar'' pattern distributions are stochastically larger than the ''wave-like'' pattern distribution. The network configuration of the ''wave-like'' pattern seems less dense than the ''rectilinear'' or ''alveolar'' patterns.

On the other hand, this feature cannot discriminate between the ''rectilinear'' and ''alveolar'' patterns. The Mann-Whitney test found no significant difference between these two patterns.

Number of regions (N_r). The number of regions is another indicator of the network density: the greater the number of regions, the denser the network (Table 1). No significant differences were found between the ''rectilinear'' and the ''wave-like'' pattern distributions. The ''alveolar'' pattern distribution was stochastically larger than the ''wave-like'' pattern distribution. Indeed, the ''alveolar'' pattern seemed to have a greater number of regions than the other patterns, although the difference was not significant ($P = 0.053$ for the Mann-Whitney test) between the ''alveolar'' pattern and the ''rectilinear'' pattern.

Mesh Structure

Areas of regions (A_r). The ''wave-like'' pattern distribution was stochastically larger than both the ''rectilinear'' and ''alveolar'' pattern distributions: the areas of regions in the ''wave-like'' patterns were the largest (Table 1). The

areas of region distributions did not show any significant difference between ''rectilinear'' and ''alveolar'' patterns.

Mean length of filaments enclosing a region (L_r). The mean length of filaments enclosing a region (L_r) can be linked to the perimeter of the mesh (Table 1). Both the ''rectilinear'' and ''wave-like'' pattern distributions were stochastically larger than the ''alveolar'' one: the perimeter in the ''alveolar'' pattern was smaller than in the other patterns. No significant differences were found between the ''wave-like'' and the ''rectilinear'' pattern distributions.

Mean elongation factor (E_f). The mean elongation factor is an indicator of mesh form (Table 1). Both the ''rectilinear'' and ''wave-like'' pattern distributions were stochastically larger than the ''alveolar'' one. The regions of ''alveolar pattern'' were less elongated than in the other patterns. The difference between the ''rectilinear'' and the ''wave-like'' pattern distributions was not significant. In both the ''rectilinear'' and the ''wave-like'' pattern, the mesh had analogue forms.

As for the mean length of filaments enclosing a region, the mean elongation factor showed that the distributions, coming from zones not located around the nucleus, were not significantly different.

Morphological Features

Curvature. The curvature distributions allow the determination of the characteristic shapes of filaments: a straight line in the ''rectilinear'' pattern, a curve in the ''wave-like'' pattern, and a circle in the ''alveolar'' pattern. For the ''rectilinear'' pattern, the curvature distribution (Fig. 5a) shows a characteristic shape which can be assimilated to the straight line. For the ''wave-like'' pattern, the distribution (Fig. 5b) is symmetrical to the y-axis. This distribution aspect is characteristic of a sinusoidal filament curve. The sum of the curvature values along a characteristic shape filament in the ''alveolar'' pattern is equal to 2π (i.e., the filament is a simply-connected closed curve), and the probability of finding a negative value is lower than 2% (Fig. 5c); the characteristic filament shape of the ''alveolar'' pattern can thus be approximated by a circle.

The Mann-Whitney test showed that the curvature distribution of the specific shape filaments in the ''alveolar'' pattern was stochastically larger than both the ''rectilinear'' and ''wave-like'' pattern distributions (Table 1). Moreover, the curvature distribution in the ''wave-like'' pattern was stochastically larger than the one in the ''rectilinear'' pattern.

Curvature, therefore, discriminates between the specific shapes depending on the patterns and, in addition to their distributions (Fig. 5), allows confirmation of the hypothesis on specific shapes: a straight line in the ''rectilinear'' pattern, a curve in the ''wave-like'' pattern, and a circle in the ''alveolar'' pattern.

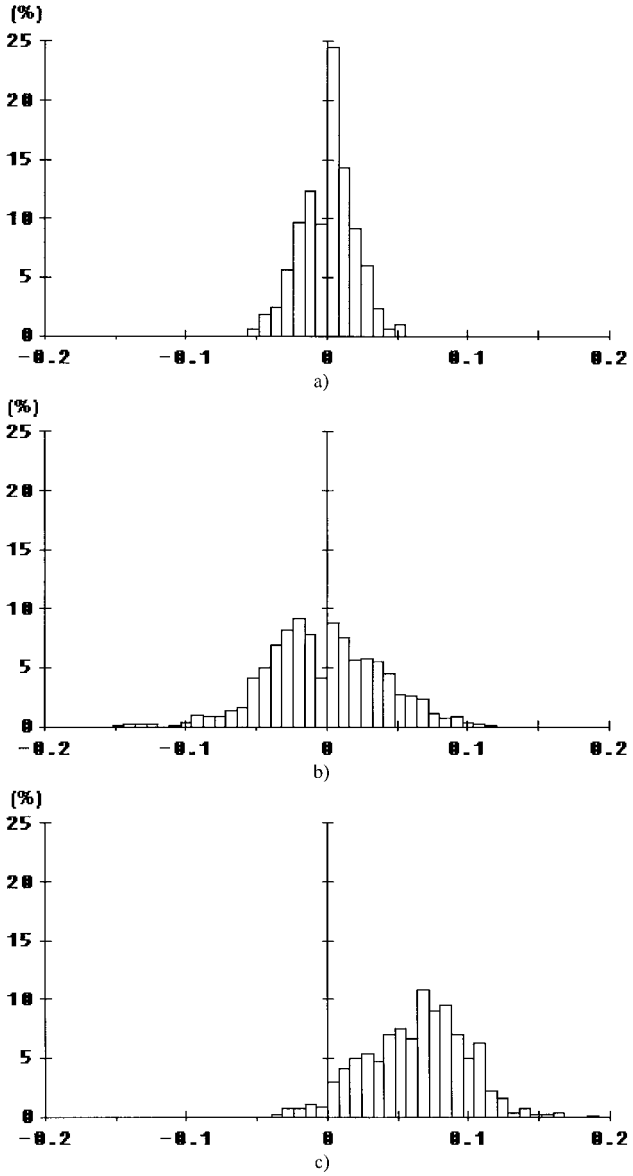

FIG. 5. Frequency distributions of the curvature values of characteristic shapes. **a:** ''Rectilinear'' pattern. **b:** ''Wave-like'' pattern. **c:** ''Alveolar'' pattern. The aspect of the curvature distributions allows the determination of characteristic shapes. a: A characteristic shape which can be likened to the straight line for the ''rectilinear'' pattern. b: Characteristic of a sinusoidal filament curve for the ''wave-like'' pattern. c: The probability of finding a negative value is lower than 2%; moreover, the sum of the curvature values along a characteristic shape filament in the ''alveolar'' pattern is equal to 2π (characteristic shape is a simply-connected closed curve); the characteristic filament shape of the ''alveolar'' pattern can thus be approximated by a circle.

DISCUSSION

This work has been focused on the quantitative analysis of cytokeratin networks whereas previous studies, dealing with both modeling and analysis of the dynamics of cytoskeletal networks, were concerned with microfilaments (34–37) or microtubules (38) at the molecular or macromolecular level.

In this paper, two methods were described to tackle the problem of analyzing networks of curvilinear objects in gray scale images. The two methods derive from different perspectives, topological and morphological. These differ-

ent perspectives allow modeling of the network at low (local) and high (global) levels of organization. Both levels are interesting because they provide complementary information concerning the variation of the network topology and of the filament morphology. Since all features must not be considered on the same level, the feature extraction is made from a particular approach. The computation of the curvature is achieved from the ''filament-approach'' results, as it requires a good approximation of the filament shape. The seven features (N_{cp}, I_c, L_f, N_r, A_r, L_r, and E_f) are determined from the combination of methods, as these features require a good estimation of both topology and morphology of the cytokeratin network.

Moreover, we observe that the ''mesh-approach'' is more efficient in isotropic zones, which are densely connected (e.g., ''alveolar'' pattern), than in anisotropic zones. The ''mesh-approach'' correctly models the topology of cytokeratin networks, but the morphology of individual filament is lost. On the other hand, the ''filament-approach'' is more efficient in anisotropic zones with a weaker connectivity (e.g., ''rectilinear'' and ''wave-like'' patterns). Therefore, the combination of methods presented here can be considered as providing an evaluation of the results of the two individual approaches. Image analysis therefore appears a powerful tool to estimate cytoskeleton architecture. Cytoskeleton segmentation could be further improved using other image analysis steps, such as differential geometry-based algorithms (39), allowing the extraction of the filament width. Our methods could be used to segment other types of filaments of cytoskeleton (microfilaments, microtubules, and vimentin) or other types of curvilinear structure networks (e.g., vessels from angiography) by adapting the parameter values, depending on the size of objects and on the mean gray scale of images.

In this work, we used confocal microscopy, rather than wide-field fluorescence microscopy, in order to increase lateral resolution for high-magnification images. On the other hand, MCF7 cultured on plastic dishes are very flat, and the sectioning capabilities of confocal microscopy were here used to analyze specific cytokeratin architecture found at specific levels, e.g., near the nuclear envelope and the substratum-cell contacts. Further generalizations of developed procedures to three-dimensional (3D) models of cytoskeletons will use the full capabilities of confocal microscopy sectioning.

In the MCF7 cell line, we observed several patterns of cytokeratin networks between isolated or confluent cells. Our hypothesis is that variations observed in the network architectures could reflect the existence of local intracytoplasmic tensions or forces, in agreement with the tensegrity paradigm of Ingber (40) or the percolation model of Forgacs (41). By means of confocal microscopy combined with image analysis, significant features, quantitating the architectural variations, are extracted and associated with the supposed intracytoplasmic forces: the ''rectilinear'' pattern appearing in the desmosome or hemidesmosome zone (''stress-force'' zone), the ''alveolar'' pattern around the nucleus maintaining nucleus position and probably protecting it from compression (''stress-force'' zone), and the ''wave-like'' pattern appearing in isolated or spreading cells in leading margin zones (''relaxed'' zone for cytokeratin filaments).

For many topological features (N_{cp}, I_c, L_f, N_r, and A_r), differences between the ''rectilinear'' and ''alveolar'' patterns are not significant. But some of them (N_{cp}, I_c, L_f, N_r, and A_r) show significant differences between the ''wave-like'' pattern and both the ''rectilinear'' and ''alveolar'' patterns. The patterns appearing in supposed ''stress-force'' zones (''rectilinear'' and ''alveolar'') show topological similarities for network density and connectivity. The cytokeratin network becomes increasingly denser and more connected in ''stress-force'' zones. Thus the connectivity and the density of the network might be modified by the occurrence of a ''stress-force'' zone. The mesh structure of the network also differs depending on the intracellular localization. The network pattern occurring around the nucleus (''alveolar'' pattern) has a mesh structure different from the other patterns (''rectilinear'' and ''wave-like''). The regions are more elongated and larger in ''rectilinear'' and ''wave-like'' than in ''alveolar'' patterns. The mesh structures of the ''rectilinear'' and the ''wave-like'' patterns are close to each other: the differences between the two patterns are not significant for either the mean elongation factor or the number of points per region.

At a lower level (morphology of elements), different characteristic filament shapes are observed: a straight line in the ''rectilinear'' pattern, a curve in the ''wave-like'' pattern, and a circle in the ''alveolar'' pattern. Curvature is a highly discriminative feature. In specific ''force-stress'' zones (desmosome or hemidesmosome), the filaments take a fixed orientation (anisotropic) and are nearly ''rectilinear.'' Around the nucleus (''alveolar'' pattern), the filaments have an isotropic configuration. In the cytoplasm, at a distance from the nucleus (''rectilinear'' and ''wave-like'' patterns), the characteristic shape is never a closed curve. Therefore, the connectivity and the density of a network describe its location in a ''stress-force'' zone or in a ''relaxed'' zone. The mesh structure characterizes the intracellular localization of the network: around the nucleus or distant from the nucleus. Moreover, the filament shape reflects the intracellular localization and the occurrence of a ''stress-force'' zone.

In conclusion, architectural variations of cytokeratin networks seem to be related to local tensions or forces appearing spontaneously in the cytoplasm of MCF7 cells in culture. However, further experiments and cytoskeleton analysis of cells submitted to external forces (work in progress) will be necessary to prove the hypothesis that the architectural variations of intermediate filaments reflect intracytoplasmic tensions.

ACKNOWLEDGMENTS

We thank Angela Downs-Rigaut and Theano Irinopoulou for helpful discussions.

LITERATURE CITED

1. Ingber DE. Tensegrity: the architectural basis of cellular mechanotransduction. Annu Rev Physiol 1997;59:575–599.
2. Thoumine O, Ott A. Time scale dependent viscoelastic and contractile regimes in fibroblasts probed by microplate manipulation. J Cell Sci 1997;110:2109–2116.
3. Thoumine O, Ziegler T, Girard PR, Nerem RM. Elongation of confluent endothelial cells in culture: the importance of fields of force in the associated alterations of their cytoskeletal structure. Exp Cell Res 1995;219:427–441.
4. Wang N, Ingber DE. Control of cytoskeletal mechanics by extracellular matrix, cell shape, and mechanical tension. Biophys J 1994;66:2181–2189.
5. Roskelley CD, Desprez PY, Bissell M. Extracellular matrix-dependent tissue-specific gene expression in mammary epithelial cells requires both physical and biochemical signal transduction. Proc Natl Acad Sci USA 1994;91:12378–12382.
6. Bissel M, Hall H, Parry G. How does the extracellular matrix direct gene expression? J Theor Biol 1982;99:31–68.
7. Maniotis A, Chen C, Ingber D. Demonstration of mechanical connections between integrins, cytoskeletal filaments, and nucleoplasm that stabilize nuclear structure. Proc Natl Acad Sci USA 1997;94:849–854.
8. Mooney D, Langer R, Ingber D. Cytoskeletal filament assembly and the control of cell spreading and function by extracellular matrix. J Cell Sci 1995;108:2311–2320.
9. Roskelley CD, Srebrow A, Bissell M. A hierarchy of ECM-mediated signalling tissue-specific gene expression. Curr Opin Cell Biol 1995;7: 736–747.
10. Getzenberg RH. Nuclear matrix and the regulation of gene expression: tissue specificity. J Cell Biochem 1994;55:22–31.
11. Pienta KJ, Coffey DS. Nuclear-cytoskeletal interactions—evidence for physical connections between the nucleus and cell periphery and their alteration by transformation. J Cell Biochem 1992;49:357–365.
12. Stewart M. Intermediate filament structure and assembly. Curr Opin Cell Biol 1993;5:3–11.
13. Janmey PA, Euteneuer U, Traub P, Schliwa M. Viscoelastic properties of vimentin compared with other filamentous biopolymer networks. J Cell Biol 1991;113:155–160.
14. Goldman RD, Khuon S, Chou YH, Opal P, Steinert PM. The function of intermediate filaments in cell shape and cytoskeletal integrity. J Cell Biol 1996;134:971–983.
15. Nagle RB. A review of intermediate filament biology and their use in pathologic diagnosis. Mol Biol Reprod 1994;19:3–21.
16. Bloom S, Lockard VG, Bloom M. Intermediate filament-mediated stretch-induced changes in chromatin: a hypothesis for growth initiation in cardiac myocytes. J Mol Cardiol 1996;28:2123–2127.
17. Curschellas E, Matter A, Regenass U. Immunolocalization of cytoskeletal elements in human mammary epithelial cells. Eur J Cancer Clin Oncol 1987;23:1517–1527.
18. Sapino A, Guidoni L, Bussolati G, Marchisio PC. Oestrogen and tamoxifen induced cytoskeletal changes in breast cancer cells. Chemioterapia 1985;4:243–245.
19. Vassy J, Millot G, Irinopoulou T, Rigaut JP, Calvo F. MCF7 cytokeratin network architecture varies according to environmental modifications. In: Abstracts of 21st Meeting of the International Association for Breast Cancer Research, Paris. 1996. p 108.
20. Beil M, Irinopoulou T, Vassy J, Wolf G. A dual approach to structural texture analysis in microscopic images. Comput Methods Programs Biomed 1995;48:211–219.
21. Vassy J, Beil M, Irinopoulou T, Rigaut JP. Quantitative image analysis of cytokeratin filament distribution during fetal rat liver development. Hepatology 1996;23:630–638.
22. Vassy J, Irinopoulou T, Beil M, Rigaut JP. Spatial distribution of cytoskeleton intermediate filaments during fetal rat hepatocyte differentiation. Microsc Res Tech 1997;39:436–443.
23. Soule HD, Vazquez J, Long A, Albert S, Brennan MA. A human cell line from pleural effusion derived from a breast carcinoma. JNCI 1973;51: 1409–1416.
24. Art J. Photon detectors for confocal microscopy. In: Pawley J, editor. The handbook of biological confocal microscopy. Madison: IRM Press; 1989. p 115–126.
25. Serra J. Image analysis and mathematical morphology. II: Theoretical advances. London: Academic Press; 1988. p 1–411.
26. Vincent L, Soille P. Watershed in digital space: an efficient algorithm based on immersion simulation. IEEE Trans PAMI 1991;13:583–597.
27. Heijmans H. Mathematical morphology: a modern approach in image processing based on algebra and geometry. SIAM Rev 1995;37:1–36.
28. Serra J. Image analysis and mathematical morphology. London: Academic Press; 1982. p 1–610.
29. Bleau A, De Guise J, Leblanc AR. A new set of fast algorithms for mathematical morphology. Identification of topographic features on grayscale images. Image Understanding 1992;56:210–229.
30. Coster M, Chermant JL. Precis d'analyse d'images. Paris: Editions CNRS; 1989. p 1–521.
31. Gray A. Modern differential geometry of curves and surfaces. Boca Raton, FL: CRC Press; 1993. p 90–95.
32. Sokal RR, Rohlf FJ. Biometry: the principles and practice of statistics in biological research. New York: Freeman; 1981. p 432–434.
33. Krickeberg K. Petit cours de statistique. Berlin, Springer-Verlag; 1996. p 34–37.
34. Civelekoglu G, Edelstein-Keshet L. Modelling the dynamics of F-actin in the cell. Bull Math Biol 1994;56:587–616.
35. Dufort P, Lumsden C. How profilin/barbed-end synergy controls actin polymerization: a kinetic model of the ATP hydrolysis circuit. Cell Motil Cytoskeleton 1996;35:309–330.
36. Satcher RL, Dewey F. Theoretical estimates of mechanical properties of the endothelial cell cytoskeleton. Biophys J 1996;71:109–118.
37. Suciu A, Civelekoglu G, Tardy H, Meister JJ. Model for the alignment of actin filaments in the endothelial cells subjected to fluid shear stress. Bull Math Biol 1997;59:1029–1046.
38. Thomason DB, Anderson O, Menton V. Fractal analysis of cytoskeleton rearrangement in cardiac muscle during head-down tilt. J Appl Physiol 1996;81:1522–1527.
39. Steger C. Extracting curvilinear structures: a differential geometric approach. Fourth European Conference on Computer Vision. Lecture Notes Comput Sci 1996;1024:630–641.
40. Ingber DE. Cellular tensegrity—defining new rules of biological design that govern the cytoskeleton. J Cell Sci 1993;104:613–627.
41. Forgacs G. On the possible role of cytoskeletal filamentous networks in intracellular signaling: an approach based on percolation. J Cell Sci 1995;108:2131–2143.

APPENDIX 1
Region-Merging Algorithm

We have designed a region-merging algorithm which erases water parting sections; it makes use of branching point detection and crest line tracking (water parting tracking). The algorithm is presented in pseudocode:

```
For each branching point (point of crest line, having more
than two neighbors belonging to crest line)
{
  For each crest line section (part of crest line from the
current branching point to the first met branching point)
  {
  Computation of the mean gray level on the crest line
  section: AL Extraction of the two adjacent region
  altitudes: A1 and A2
  If |A1-A2| < R Then
       {
       If min (|AL-A1|, |AL-A2|) < M Then
            {
            Erase the crest line section
            }
       }
}
```

R is the criterion of region to region proximity, and M is the criterion of region to frontier proximity; R and M are empirical parameters. In our images, R and M are equal to 15 (Fig. 2g–i).

APPENDIX 2
Nonlinear Filter of the "Filament-Approach"

In the selection step, for each pixel, in a neighborhood centered around itself, the number of neighbors N_{xy} whose gray value is lower or equal than the current pixel

value and S_{xy} the number of neighbors whose gray value is equal to the current pixel value are computed.

Let $I(x,y) = z_{xy}$, where z_{xy} is the gray level at position (x,y),

$$\forall (x, y)$$

$$N_{xy} = \sum_k \sum_l N_{x+ky+1}, \quad \text{with } N_{x+ky+1}$$

$$= \begin{cases} 1 & z_{xy} \geq z_{x+ky+1} \\ 0 & z_{xy} < z_{x+ky+1} \end{cases}, \; k \in \{-n, \ldots, n\}, \; 1 \in \{-n, \ldots, n\},$$

$$S_{xy} = \sum_k \sum_l S_{x+ky+1}, \text{ with } S_{x+ky+1}$$

$$= \begin{cases} 1 & z_{xy} = z_{x+ky+1} \\ 0 & z_{xy} \neq z_{x+ky+1} \end{cases}, \; k \in \{-n, \ldots, n\}, \; 1 \in \{-n, \ldots, n\};$$

The neighborhood size ($(2n + 1)^2$) depends on the width of the objects in the images: the curvilinear element must fit in the selection mask. Therefore, if the curvilinear objects have a mean width of 7 pixels (Fig. 1c–e), a window of size 9×9 pixels will be used.

In the decision step, we decide if the pixel is a local element of a ridge, with the help of decision criterion δ, and if the pixel belongs to a blurred zone with decision criterion θ. If a pixel is considered as a ridge element and does not belong to a blurred zone, it is preserved taking into account its neighborhood, i.e., a smoothing, with smaller mask size ($(2m + 1)^2$, $m < n$), is applied in order to reduce noise before writing this pixel in the new image I^N.

$$\text{If } (N_{xy} > \delta \text{ and } S_{xy} < \theta) \quad \text{then } z^N_{xy} = \overline{z_{xy}}\,(x, y) \text{ is a local optimum (smoothing)}$$
$$\text{else } z^N_{xy} = 0 \; (x, y) \text{ is not preserved (thresholding)}$$

with

$$\overline{z_{xy}} = \frac{1}{(2m + 1)^2} \sum_i \sum_j z_{x+iy+j}, \qquad i \in \{-m, \ldots, m\}, \quad j \in \{-m, \ldots, m\};$$

$\sqrt{\delta}$ must be equal to the mean width of the objects in such a way that δ roughly represents the object area included in the selection mask. In Figure 3a–c, δ is equal to 49.

Therefore, θ is the detector of blurred zones (cytoplasmic gel zones or zones not belonging to the focal plane); $\sqrt{\theta}$ must be larger than the object width in order to avoid deleting too many object-points. In Figure 3a–c, θ is equal to 60. The smoothing neighborhood size ($(2m + 1)^2$) depends on the mean width of the objects in the images: the neighborhood must be included in the curvilinear element. Therefore, if the curvilinear objects have a mean width of 7 pixels (Fig. 1c–e), a window of size 3×3 pixels will be used.

The filter Ψ detects ridges (crest line neighborhoods). It is a selective smoothing adaptive filter which operates a smoothing on zones satisfying a criterion (selective smoothing) and uses two different mask sizes (adaptive). It implements variable size masks depending on step ($(2n + 1)^2$ for the selection and $(2m + 1)^2$ for the smoothing) and it includes a decision stage.

APPENDIX 3
Reconstruction of the Curvilinear Elements in the "Filament-Approach"

For each threshold value

{

Inf = $(1 - \tau) \times$ Threshold
Sup = $(1 + \tau) \times$ Threshold
For each $z_{xy} \in$ [Threshold, Sup]
{

$$C_{xy} = \sum_k \sum_l C_{x+ky+1}$$

$$C_{x+ky+1} = \begin{cases} 1 & z_{x+ky+1} \in \text{[Inf, Threshold]} \\ 0 & z_{x+ky+1} \notin \text{[Inf, Threshold]} \end{cases}$$

If $C_{xy} > \phi$ then z_{xy} is marked (determination of maxima of image zones corresponding to the interval [Threshold, Sup])

}

Dilation of the marked zones by a circle (in order to connect two one-pixel-distant maxima)

Binary skeletonization (to obtain a unit-size width line)

}

The basis of the decision domain is a neighborhood whose size depends on the mean width of the objects: the neighborhood must be included in the object. In Figure 3a–c, the preprocessed objects have a mean width of 5 pixels, so the neighborhood size is 3×3. τ allows the variability of the depth of decision domain [Inf,Threshold]. The τ value depends on the mean gray level of the images. The lower the mean gray level, the higher the τ value.

Mean gray levels	τ	
115	0.2	Figure 1c
65	0.3	Figure 1e
45	0.35	Figure 1d

The selected pixels, according to the criterion ϕ , are marked; ϕ is an empirical parameter, equal to 5 in Figure 3d–f. The circular dilation step allows the restoration of connectivity without favoring a specific direction. The structuring element must be included in the preprocessed object; thus, the structuring element size is 3×3. The binary skeletonization is applied on the dilated marked zones by taking the successive skeletons (Fig. 3d–f).